

# DEVELOPMENT OF NUMERICAL TECHNIQUES FOR NEAR-FIELD AEROACOUSTIC COMPUTATIONS

G. DJAMBAZOV, C.-H. LAI AND K. PERICLEOUS\*

*Centre Numerical Modelling, University of Greenwich, London SE18 6PF, UK*

## SUMMARY

This work is concerned with the development of a numerical scheme capable of producing accurate simulations of sound propagation in the presence of a mean flow field. The method is based on the concept of variable decomposition, which leads to two separate sets of equations. These equations are the linearised Euler equations and the Reynolds-averaged Navier–Stokes equations. This paper concentrates on the development of numerical schemes for the linearised Euler equations that leads to a computational aeroacoustics (CAA) code. The resulting CAA code is a non-diffusive, time- and space-staggered finite volume code for the acoustic perturbation, and it is validated against analytic results for pure 1D sound propagation and 2D benchmark problems involving sound scattering from a cylindrical obstacle. Predictions are also given for the case of prescribed source sound propagation in a laminar boundary layer as an illustration of the effects of mean convection. Copyright © 1999 John Wiley & Sons, Ltd.

KEY WORDS: sound propagation; sound scattering; aeroacoustics

## 1. INTRODUCTION

The generation and propagation of sound due to the presence of a mean flow field is a physical problem of great interest to engineers and environmentalists. In view of the great advance of computational techniques in the solution of complex fluid flow problems of practical interest, there is an expectation that similar success can be achieved in the solution of the problem of aeroacoustics. There are many practical instances where reliable and easy to apply computational aeroacoustic (CAA) techniques would be of great value. Example applications include the noise problem in the vicinity of airports, the problem of noise pollution surrounding the exit of busy road tunnels, the design of vehicle exhaust systems, the suppression of shear-generated sound from high speed air jets. There are also other areas, where sound itself is not a problem; controlled application of sound waves can be used to some benefit, e.g. to improve boundary layer stability, or to design Doppler effect anemometers.

Unfortunately, in spite of the rapid advance of computers, the direct computation of acoustic fields generated by flow remains an intractable problem. For example, if the ecologically important zone near an airport covering the take-off or landing of an aircraft is assumed to be 300 m long, by 300 m wide by 100 m high, then even for the lowest frequency range of interest, say 100 Hz, a conservative resolution requirement of 10 points per wavelength, would imply 236 million grid points! Also the acoustic energy in a flow field is

---

\* Correspondence to: Centre Numerical Modelling, University of Greenwich, London SE18 6PF, UK.

often only an insignificant fraction of the total energy present. As a consequence, the pressure–density perturbations responsible for sound travel are invariably swamped by the mean flow quantities.

This latter realisation led to the development of the classical means of computing aeroacoustic fields, Lighthill's acoustic analogy [1], which relies on the separation of the acoustic perturbations and the solution of the resulting linearised Euler equations. This technique has been used as a complement to recent studies of the propagation of sound generated by isotropic turbulence [2] and for the far-field noise radiation from an acoustic cavity [3]. Since only the region in the vicinity of the sound source is non-linear, it is possible to divide the area of interest into near-field and far-field zones [2,4]. Special high accuracy wave transport methods can be applied to the far field [5], or alternatively the Kirchoff surface integral method [6,7] may be used.

The problem still remains on how to model the near-field region, which has to be large enough to contain all the non-linearities of the sound field. This region, which may still reach 100 or more wavelengths from the source of sound, is more manageable in terms of computer resources. Extending the idea of Lighthill, the problem is decomposed into mean flow and sound perturbation quantities, but the non-linear terms in the equations containing contributions due to viscosity and mean flow gradients are retained (e.g. Hardin [8], Viswanathan *et al.* [9] and Djambazov [10]). It remains to ensure that the sound signal is not attenuated by numerical diffusion within this region. The authors have shown how a number of numerical schemes perform in this respect in an earlier communication [11].

In view of the fact that most CFD fluid flow codes use finite volume type discretisation, in the present contribution, the authors detail the development of a finite volume CAA technique for the near-field region, which can easily interface to standard CFD mean flow codes. The remainder of the paper describes the new method, shows validation examples in cases where the non-linear terms in the equations are unimportant and also illustrates simple flow examples where interaction with the mean flow field influences sound propagation. Finally, the potential of the method as a practical tool in predicting and transporting sound information in a real flow field is demonstrated by modelling the sound generated by the impact of a convected vortex onto a stationary solid plate.

## 2. THE METHOD USED

### 2.1. Variable decomposition

Sound is a form of fluid motion, and it is therefore governed by the equations of continuity and momentum conservation. If you assume sound appears as a perturbation of the mean flow field, then any fluid quantity can be expressed as the sum of a mean value (denoted by the subscript 0) and a perturbation value. Assuming index summation convention, the equations of motion can be written as

$$\frac{\partial(\rho_0 + \rho)}{\partial t} + \frac{\partial}{\partial x_j} [(\rho_0 + \rho)(u_{j0} + u_j)] = S, \quad (1)$$

$$(\rho_0 + \rho) \left[ \frac{\partial(u_{i0} + u_i)}{\partial t} + (u_{j0} + u_j) \frac{\partial(u_{i0} + u_i)}{\partial x_j} \right] + \frac{\partial(p_0 + p)}{\partial x_i} = F_{i0} + F_i. \quad (2)$$

The symbols  $\rho$ ,  $u_i$  and  $p$  denote respectively, the fluid density, velocity and pressure perturbation, while  $F_{i0}$  and  $F_i$  contain both external forces and internal viscous friction in the mean

flow and perturbations respectively.  $S$  denotes external sources of sound that can either be due to vibrating solid objects, or alternatively represent aerodynamic disturbances that may be extracted from the fluctuating pressure field in a time-dependent CFD computation [12].

As explained above, this variable decomposition allows a separate treatment between the large scale mean flow motion and the small sound perturbations superimposed upon it. For example, existing CFD codes can still be used to solve the 'mean flow'. Although for a typical aeroacoustic problem, terms containing perturbations may be comparatively small, terms containing the derivatives of perturbations are not necessarily so. After simplification, subtraction of the mean flow equations, and with all the small terms moved to the right-hand-side, (1) and (2) become

$$\frac{\partial \rho}{\partial t} + u_{j0} \frac{\partial \rho}{\partial x_j} + \rho_0 \frac{\partial u_j}{\partial x_j} = q, \quad (3)$$

$$\rho_0 \left( \frac{\partial u_i}{\partial t} + u_{j0} \frac{\partial u_i}{\partial x_j} \right) + \frac{\partial p}{\partial x_i} = f_i, \quad (4)$$

where

$$q = S - \left[ \rho \frac{\partial}{\partial x_j} (u_{j0} + u_j) + u_j \frac{\partial}{\partial x_j} (\rho_0 + \rho) \right], \quad (5)$$

$$f_i = F_i - \rho \frac{\partial}{\partial t} (u_{i0} + u_i) - [\rho_0 u_j + \rho (u_{j0} + u_j)] \frac{\partial}{\partial x_j} (u_{i0} + u_i). \quad (6)$$

These are the governing equations for the perturbation part of the near-field. With the mean flow values computed by a CFD code, the left-hand-side is linear and the small right-hand-side can be obtained iteratively.

The sequential interaction between CFD and CAA is pictured in Figure 1. It is generally assumed that feedback of the sound on the flow field is only to be expected when there is a resonator nearby [1], as denoted by the dotted line. In most cases, iteration in the outermost loop is not necessary. The structured CFD code PHOENICS [13] and the unstructured code PHYSICA [14] have been used in this study.

#### Mean flow:

$$\frac{\partial \rho_0}{\partial t} + \frac{\partial}{\partial x_j} (\rho_0 u_{j0}) = 0$$

$$\rho_0 \left( \frac{\partial u_{i0}}{\partial t} + u_{j0} \frac{\partial u_{i0}}{\partial x_j} \right) + \frac{\partial p_0}{\partial x_i} = F_{i0}$$

#### Acoustic perturbation:

$$\frac{\partial \rho}{\partial t} + u_{j0} \frac{\partial \rho}{\partial x_j} + \rho_0 \frac{\partial u_j}{\partial x_j} = q$$

$$\rho_0 \left( \frac{\partial u_i}{\partial t} + u_{j0} \frac{\partial u_i}{\partial x_j} \right) + \frac{\partial p}{\partial x_i} = f_i$$

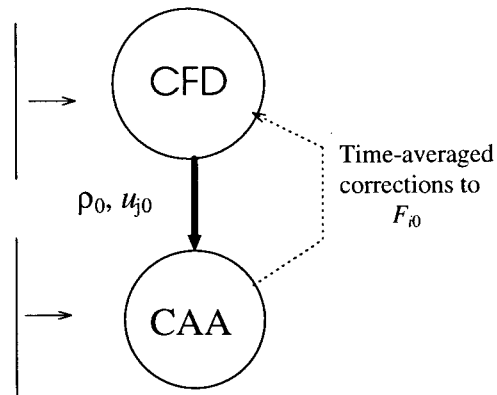


Figure 1. Interaction between CFD and CAA codes.

The coupling can be effected in two ways:

1. Following [12], the full perturbation field is solved, with the sound sources defined in a somewhat artificial way on the basis of the pressure oscillations that appear in the CFD solution.
2. Solve for the differences between the true physical fields of pressure, velocity and density, and the ones computed by the CFD code. The acoustic signal will then be extracted by post-processing the sum of the CFD and CAA solutions.

In both cases, the appropriate perturbation equations are the linearised Euler equations (3) and (4), complemented with a pressure–density relation. The first option is described by Equations (5) and (6).

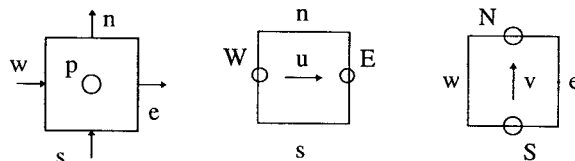
## 2.2. Pure propagation

The non-linearities in the equations presented are partly due to the presence of viscous terms and partly due to the presence of a mean flow field. If the usual inviscid assumption can be made and if the mean flow field is uniform, a moving frame of reference can be used to eliminate the non-linear terms. The result is a set of equations for pure sound propagation. Then, Equations (3) and (4) can be expressed in a slightly different form, using the standard definition for the speed of sound  $c$ , under adiabatic conditions as shown below in two dimensions:

$$\begin{aligned} \frac{\partial p}{\partial t} + c \left( \frac{\partial u}{\partial x} + \frac{\partial v}{\partial y} \right) &= q, \\ \frac{\partial u}{\partial t} + c \frac{\partial p}{\partial x} &= f_1, \quad u = \rho_0 c u_1, \\ \frac{\partial v}{\partial t} + c \frac{\partial p}{\partial y} &= f_2, \quad v = \rho_0 c u_2, \\ \frac{\partial p}{\partial \rho} &= c^2 = \gamma \frac{p_0}{\rho_0}, \quad \gamma_{\text{air}} = 1.4. \end{aligned} \quad (7)$$

Here  $u_1$  and  $u_2$  are the Cartesian components of the velocity vector. The right-hand quantities are assumed to be known functions of the independent variables  $x$ ,  $y$  and  $t$ .

A fully staggered grid (in both space and time) has been used to discretise these equations. As shown below, a fully explicit stable second-order-accurate scheme results. This can be extended if needed to third-order-implicit, whilst at the same time retaining diagonal dominance for stability and fast convergence.



Using the cell-centred regular Cartesian mesh and the notation shown, a finite volume set of equations has been obtained by successive integration of Equations (7) along each of the axes  $x$ ,  $y$  and  $t$ :

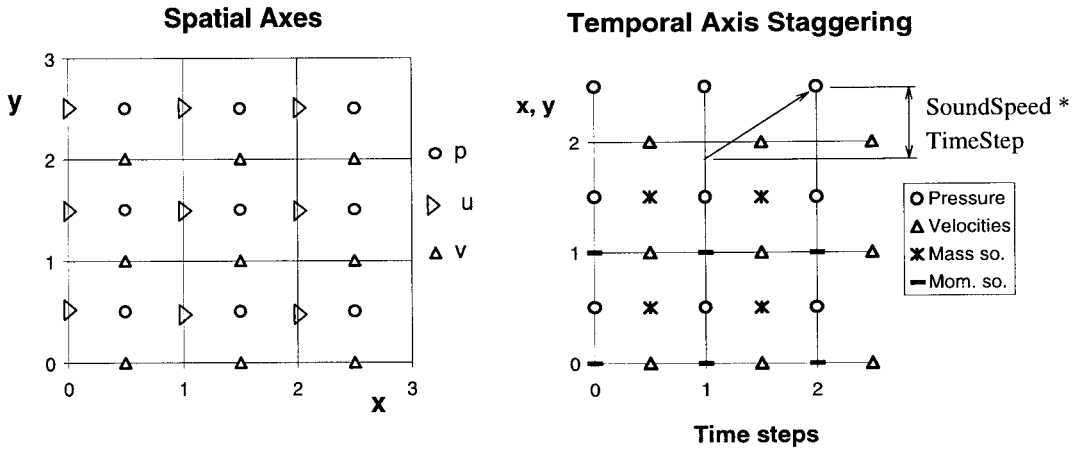


Figure 2. Computational grid and radiating boundary interpolation.

$$\begin{aligned}
 & \int_{\text{cell}} (p - p_{\text{old}}) dx dy + c \left[ \int_{\text{old}}^{\text{new}} dt \int_s^n (u_e - u_w) dy + \int_{\text{old}}^{\text{new}} dt \int_w^e (v_n - v_s) dx \right] \\
 & = \int_{\text{old}}^{\text{new}} dt \int_{\text{cell}} q dx dy, \\
 & \int_{\text{cell}} (u - u_{\text{old}}) dx dy + c \int_{\text{oldM}}^{\text{newM}} dt \int_s^n (p_E - p_W) dy = \int_{\text{oldM}}^{\text{newM}} dt \int_{\text{cell}} f_x dx dy, \\
 & \int_{\text{cell}} (v - v_{\text{old}}) dx dy + c \int_{\text{oldM}}^{\text{newM}} dt \int_w^e (p_N - p_S) dx = \int_{\text{oldM}}^{\text{newM}} dt \int_{\text{cell}} f_y dx dy.
 \end{aligned} \tag{8}$$

The solved for values of pressure are stored in the cell centres (with uppercase indices), while the velocities are stored on cell faces (lowercase indexes) in the middle of each time step ( $t_{\text{oldM}} = t_{\text{old}} + \Delta t/2$ ,  $t_{\text{newM}} = t_{\text{new}} + \Delta t/2$ ). The storage locations are shown in Figure 2.

The finite volume equations (8) can be used to define either second- or higher-order numerical schemes for the solution of (7). The integrals in (8) are first evaluated through mean values, providing an easy-to-program, second-order-accurate, fully explicit numerical scheme:

$$\begin{aligned}
 p &= p_{\text{old}} - \sigma_x(u_e - u_w) - \sigma_y(v_n - v_s) + q\Delta t, \\
 u &= u_{\text{old}} - \sigma_x(p_E - p_W) + f_1\Delta t, \\
 v &= v_{\text{old}} - \sigma_y(p_N - p_S) + f_2\Delta t, \\
 \sigma_x &= \frac{c\Delta t}{\Delta x}, \quad \sigma_y = \frac{c\Delta t}{\Delta y}.
 \end{aligned} \tag{9}$$

The scheme is accurate to within 5 wavelengths, with maximum errors reaching 8% of amplitude (see Djambazov *et al.* [11]). To extend the accuracy, a second-order approximation of all the functions in the integrals of (8) was introduced. Instead of  $I(x_0, h) = hf(x_0)$ , we now have

$$I(x_0, h) = \int_{x_0-h/2}^{x_0+h/2} f(x) dx = h[Af(x_0-h) + (1-2A)f(x_0) + Af(x_0+h)], \quad A = \frac{1}{24}, \tag{10}$$

applied to all integrals. In 2D, this means

$$\int_{\text{cell}} f(x, y) \, dx \, dy = \left[ A \sum_{\text{nb}} f_{\text{nb}} + (1 - 4A) f_{\text{cell}} \right] \Delta x \, \Delta y, \quad (11)$$

with 'nb' used to denote all four neighbouring cells.

This semi-implicit scheme proved to be accurate enough to take the sound generated out of the 'near-field', since as shown in Figure 3, even after 100 wavelengths, the initial pulse is captured quite accurately, with the maximum amplitude error being about 5%. The solution shown was obtained for a Courant number  $\sigma_x = c\Delta t/\Delta x = 0.7$  [11].

Since the scheme is now partly implicit, the complete system of linear equations needs to be solved at each time step. Due to the large number of grid points, direct methods of solution cannot be considered appropriate. An iterative scheme has been developed instead, which uses the explicit solution as the initial guess. In practice it was found that for purely linear problems, 2–4 iterations are sufficient for convergence. Where the non-linear terms on the right-hand-side of the equation are present, more iterations are necessary; these are run concurrently with the linear system.

The advantage of the present scheme over other more accurate higher-order schemes is that it employs only one level of neighbouring cells. This allows easy extension to three dimensions and simplifies the treatment of boundaries, especially where complex solid shapes are present within the solution domain—the explicit scheme is then used locally.

An implication of the time staggering approach, is that 'future' and 'past' neighbours need to be computed at each time step, using the explicit scheme. Stored 'past' values cannot safely be used, because of the Courant limit when the time step is adjusted to whole cells.

Acoustic radiation boundary conditions are implemented at open boundaries, assuming plane wave propagation. Velocity components at the boundary faces are computed from the velocity field at the previous step, by interpolation at the appropriate points inside the domain (see Figure 2). The direction of radiation has then to be prescribed for each boundary cell. The distance the wave covers in one time step determines the position of the interpolation point.

Solid boundaries are represented in a stepwise manner as shown in Figure 4. The corresponding velocity components perpendicular to the boundary cell faces are set to zero. Although the approximation of the solid surface is not ideal, this does not affect significantly

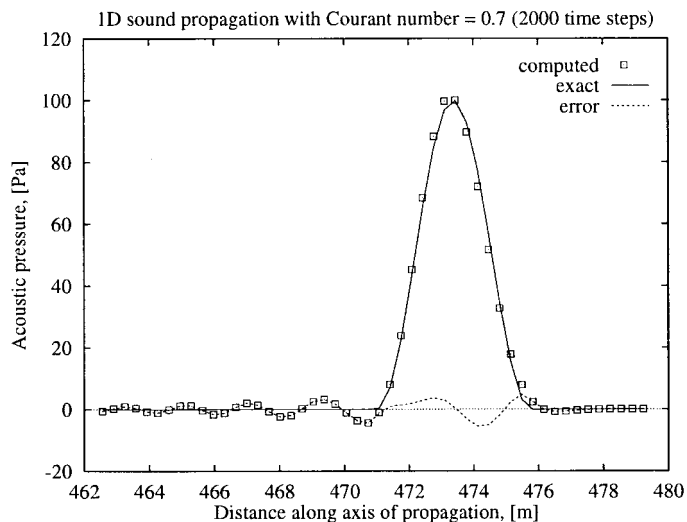


Figure 3. The semi-implicit scheme; test pulse after travelling 100 wavelengths.

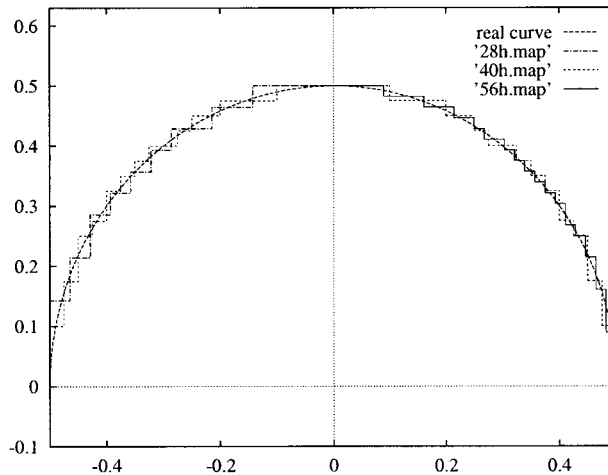


Figure 4. Solid boundary—stepwise representation showing the effects of mesh refinement.

the acoustic results (it can be seen in Figure 9(a) that the errors in the reflected pulse in the middle of the graph are not larger than the errors in the main pulse to the left of the graph). Of course, with the mean flow solution, the solid boundaries have to be represented as smooth.

A measure of the accuracy of the method described above can be seen in its application to a recent benchmark exercise [15], which will be described in Section 3.

### 2.3. Modelling convection

Where the mean flow field  $(u_0, v_0)$  is not uniform, careful attention needs to be paid to the convection terms in Equations (3) and (4) to achieve the accuracy required in aeroacoustic computations. In [11], a number of schemes were compared, including upwind-explicit, MacCormack–Lax–Wendroff, the van Leer–TVD explicit and upwind–downwind implicit [16]. The last of these was selected to be combined with the pure propagation scheme described earlier, as it has the same accuracy and its finite volume formulation remains conveniently space-centred. The scheme is given by the following equation:

$$\left(1 - \frac{\sigma}{2}\right)p + \frac{\sigma}{2}p_{\text{downwind}} = \left(1 - \frac{\sigma}{2}\right)p^{\text{old}} + \frac{\sigma}{2}p_{\text{upwind}}^{\text{old}}, \quad (12)$$

where  $\sigma = u_0 \Delta t / \Delta x$  is the Courant number.

An example application of the full-linearised Euler equations is presented in the next section.

## 3. APPLICATIONS

### 3.1. The acoustic scattering benchmark problems

The acoustic propagation module was applied to the following two problems, which were set at the recent *Computational Aeroacoustics Workshop on Benchmark Problems*, in Tallahassee, FL [15].

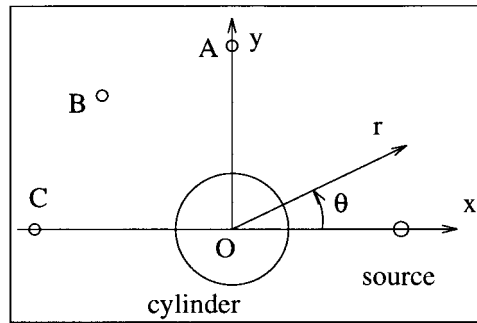


Figure 5. Sketch of Problem 1.

### Problem 1

The physical problem concerns the sound field generated by a propeller scattered off the fuselage of an aircraft. The pressure loading on the fuselage is of interest as an input to the interior noise problem. The benchmark was set to test in particular, the accuracy of curved boundary conditions, which in this work were modelled in a stepwise fashion (Figure 4).

The idealised fuselage and noise source position are shown in Figure 5. The source of sound is prescribed as follows:

$$S = \exp\left[-\ln 2\left(\frac{(x-4)^2 + y^2}{(0.2)^2}\right)\right] \sin \omega t, \quad (13)$$

with  $\omega = 8\pi$ .

Results were to be compared against the benchmark solution, which was not known beforehand at positions A, B and C.

A uniform Cartesian grid of up to  $800 \times 400$  cells was used for this benchmark, over a domain of approximately  $14 \times 7$  units (Figure 6). The cell size was 0.01786 units, and the time

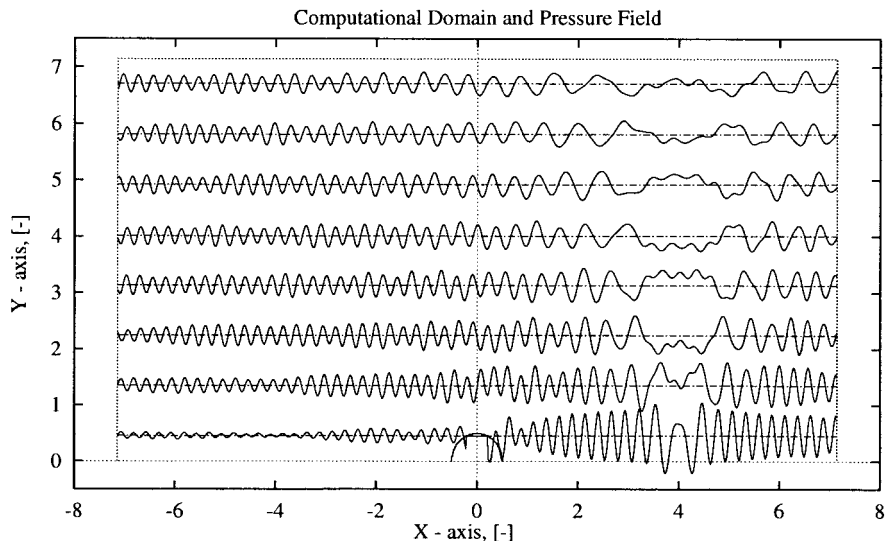


Figure 6. Computational domain and instantaneous pressure field for Problem 1.

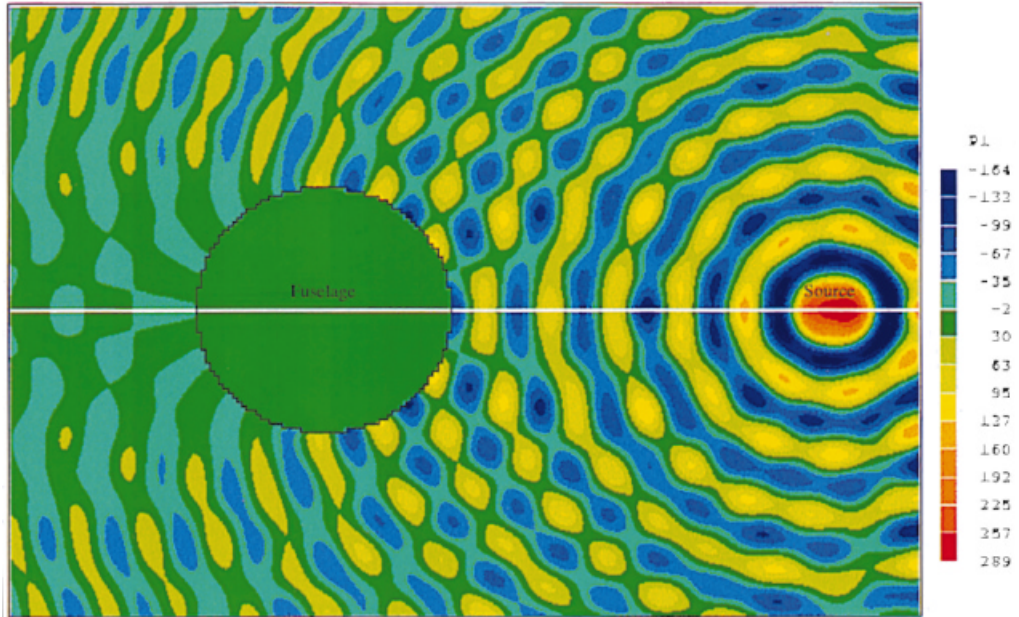


Plate 1. Contours of instantaneous pressure showing interference patterns caused by the interaction of emitted waves from the source and reflected waves from the cylinder.

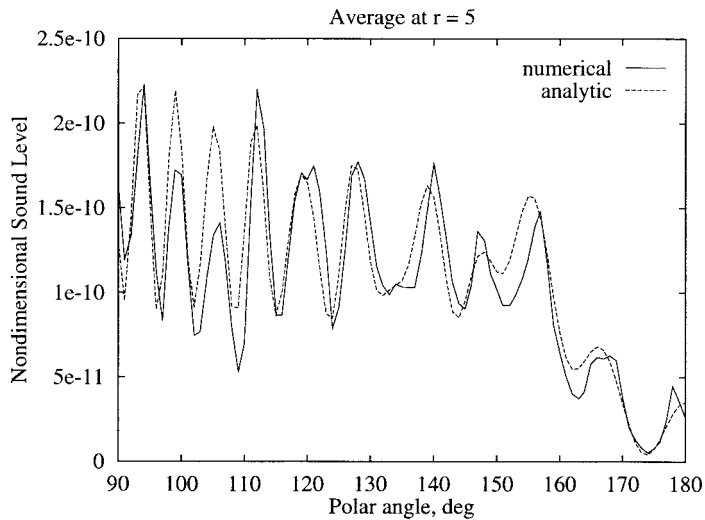


Figure 7. Comparison between numerical and benchmark solutions for Problem 1, at  $r = 5$ .

step 0.0125 units (normalised with respect to  $D/c$ , the cylinder diameter over the sound speed). The instantaneous pressure field generated by the sound source is shown in Figure 6. The distance between the cylinder and source is an integer number of wavelengths, leading to the creation of a standing wave between them. A sound 'shadow' is evident at the rear of the cylinder. The successive amplification/attenuation of the sound signal as the emitted and reflected signals meet, is better seen in Plate 1, which shows an instantaneous map of the pressure throughout the domain.

The benchmark solution, published in [17], was analytical and independent of radius for  $r \rightarrow \infty$ . The numerical solution, however, can only be realised for a finite radius; for this

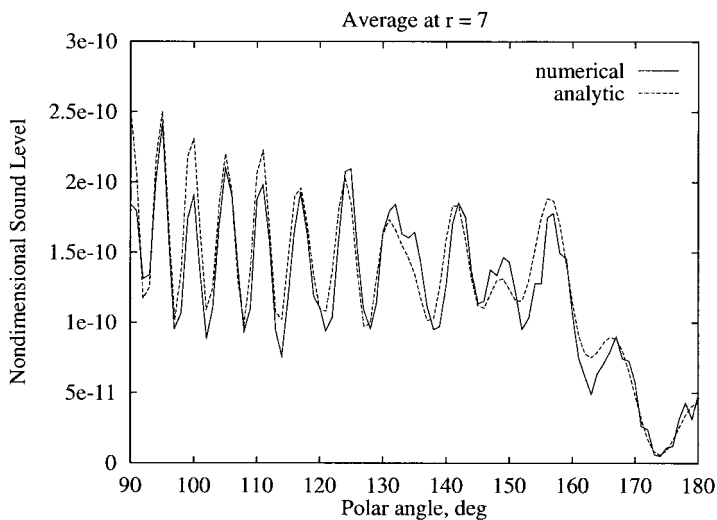


Figure 8. Comparison between numerical and benchmark solutions for Problem 1, at  $r = 7$ .

reason, results were produced for comparison by taking the square of the pressure at two radii,  $r = 5$  and  $r = 7$ . A comparison of the computed and analytical results is shown in Figures 7 and 8 below. There is a close correlation between the two results, with the  $r = 7$  solution being the closer of the two as expected.

### Problem 2

This is the same as Problem 1, except that there is no time periodic source, i.e.  $S = 0$ . Instead, an initial pressure pulse is specified which then propagates in time. This is then an initial value problem, with  $u = v = 0$  at  $t = 0$ , and

$$p = \exp \left[ -\ln 2 \left( \frac{(x-4)^2 + y^2}{(0.2)^2} \right) \right]. \quad (14)$$

The same grid spacing ( $h = D/56$ ), time step ( $\Delta t = 0.01$ ) and solid boundary mapping as with Problem 1 were used, but the extent of the domain was reduced to  $600 \times 300$  cells—enough to contain the target semicircle of radius  $r = 5$  units.

Solutions are compared with the analytical ones at three points, A ( $r = 5$ ,  $\theta = 90^\circ$ ), B ( $r = 5$ ,  $\theta = 135^\circ$ ), C ( $r = 5$ ,  $\theta = 180^\circ$ ), as shown in Figure 9(a)–(c). The computations in this case were performed using three different meshes to check grid dependence of the results ( $h = D/40$  and  $h = D/28$ ). In all three cases, the mesh is fine enough to resolve the pressure pulse, but the stepwise discretisation of the cylinder is different (see Figure 4).

Comparison between the benchmark and numerical solutions shows that the technique predicts the passage of the pressure pulse over the obstacle quite accurately. However, and quite surprisingly, the coarser mesh seems to give a better agreement with the benchmark results in position A, at right angles to the cylinder. It appears that the finest mesh introduces high frequency oscillations to the solution. These oscillations are almost certainly due to a correlation between the pulse wavelength and the cylinder wall step size.

Typical times for these runs on a Sun Sparc 20 workstation are, 1 h for the coarse mesh, 3 h for the medium mesh and 10 h for the fine mesh. This indicates an approximately linear relationship between mesh size and computational time.

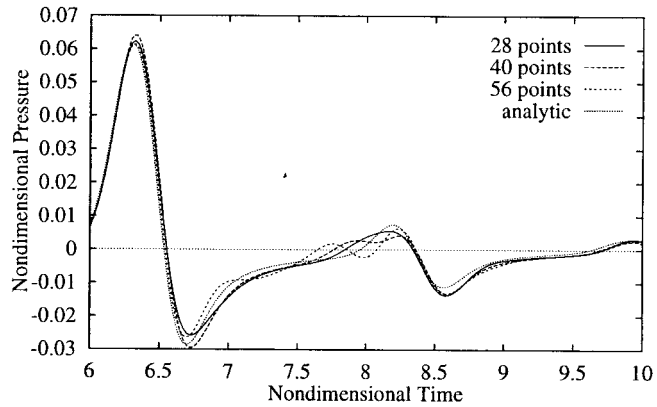
### 3.2. Boundary layer convection test

To test the performance of the CAA module in the presence of non-uniform convection, the problem depicted in Figure 10 was addressed. It concerns the propagation of a sound wave through a laminar boundary layer on a flat plate. A point source on the plate surface simulates a vibrating diaphragm, introducing a displacement pulse on the surface.

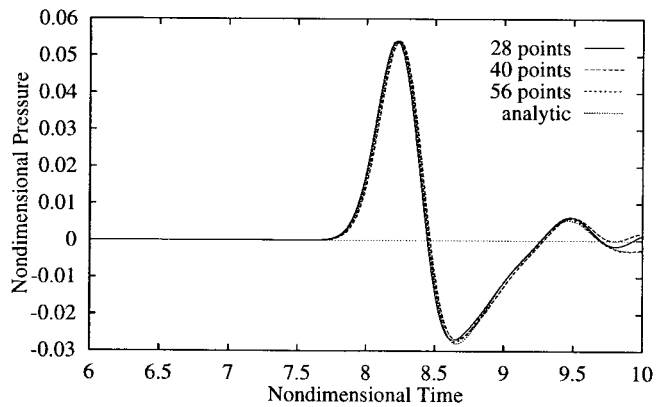
The boundary layer velocity profile is assumed to be the one plotted with solid line in the right graph of Figure 10. In a real coupled simulation, the CFD domain can be smaller than the acoustic one in order to reduce the computational cost. Then uniform mean flow is assumed outside the CFD region.

Phase displacement of the signal propagating in a boundary layer is observed (relative to the signal in a uniform flow), which is a function of the mean velocity magnitude. The pressure perturbation is 'compressed' upstream of the source, and 'expanded' downstream as expected. The reciprocal effect, i.e. the influence of the sound wave on the boundary layer development, has not been addressed—it remains the subject of future study.

(a) Time history of point A ( $r = 5, \theta = 90^\circ$ )



(b) Time history of point B ( $r = 5, \theta = 135^\circ$ )



(c) Time history of point C ( $r = 5, \theta = 180^\circ$ )

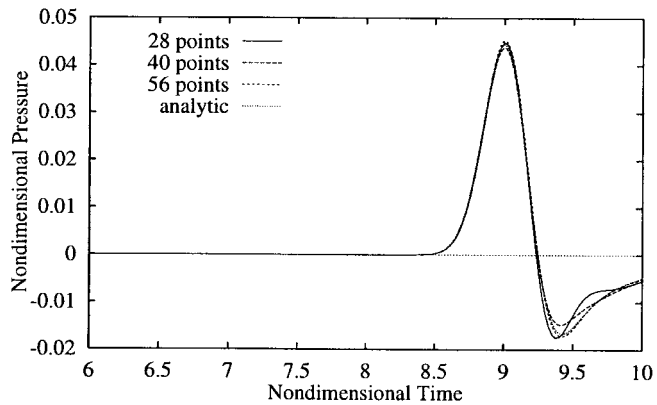


Figure 9. Problem 2 solution, comparison between numerical and analytical solution, and effect of mesh density; (a) time history of point A ( $r = 5, \theta = 90^\circ$ ), (b) time history of point B ( $r = 5, \theta = 135^\circ$ ), (c) time history of point C ( $r = 5, \theta = 180^\circ$ ).

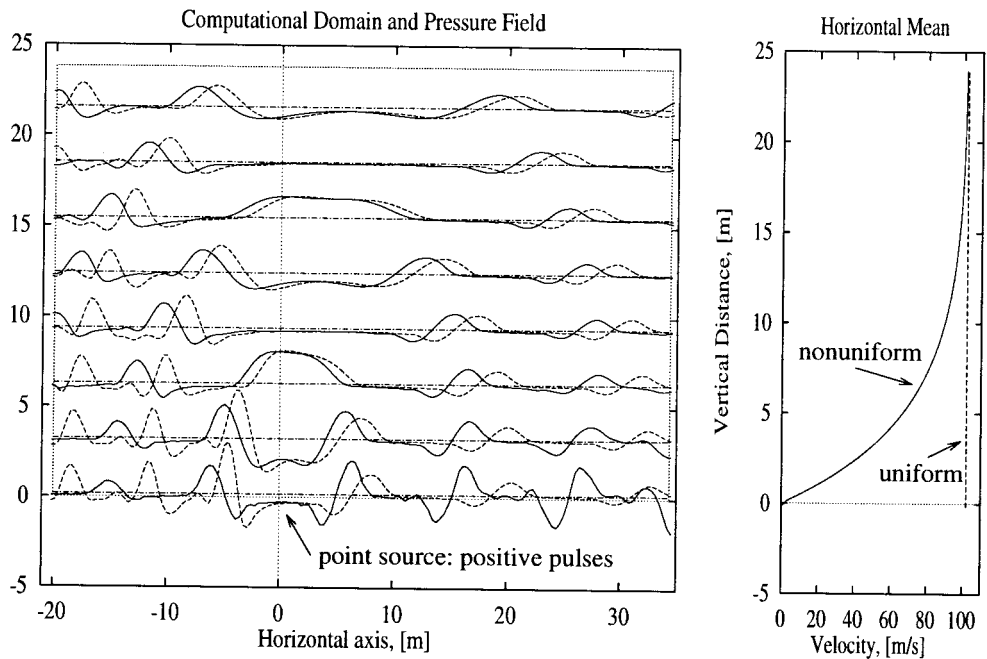


Figure 10. Acoustic perturbation travel in a boundary layer (solid lines) and in a uniform mean flow (broken lines).

#### 4. CONCLUDING REMARKS

In this work a novel finite volume technique featuring time and space staggering has been developed, to address the problem of aeroacoustic computation. The technique is capable of computing the propagation of acoustic signals through an arbitrary flow field using a tandem CFD-CAA code arrangement.

Propagation of signals of known frequency has been demonstrated with minimum attenuation at up to 100 wavelengths away from the source.

The treatment of obstacles using cell blockages has been shown to be feasible even for curved boundaries. However, comparison with benchmark solutions has shown that careless choice of step-to-wavelength ratio can lead to higher frequency errors.

Sources of sound have been prescribed in all cases considered here. However, work is in progress to compute the generation of aerodynamic sound by flow features, such as the interaction of a convected vortex with a solid obstacle placed in its path. Preliminary results of this work appeared at a recent conference [12].

#### REFERENCES

1. J.M. Lighthill, 'On sound generated aerodynamically: I. General theory', *Proc. R. Soc. A*, **211**, 564–587 (1952).
2. S. Sarkar and M.Y. Hussaini, 'A hybrid direct numerical simulation of sound radiated from isotropic turbulence', in R.R. Mankbadi *et al.* (eds.), *Computational Aero- and Hydroacoustics*, vol. FED-147, ASME, 1993, pp. 83–89.
3. X. Zhang, A. Rona and G.M. Lilley, 'Far-field noise radiation from an unsteady supersonic cavity flow', in *1st CEAS/AIAA Aeroacoustics Conference, No. 95-040*, 1995.
4. S.H. Shih, D.R. Hixon and R.R. Mankbadi, 'A zonal approach for prediction of jet noise', in *1st CEAS/AIAA Aeroacoustics Conference, No. 95-144*, 1995.
5. C.K.W. Tam and J.C. Webb, 'Dispersion relation preserving finite difference schemes for computational acoustics', *J. Comput. Phys.*, **107**, 262–281 (1993).

6. A.S. Lyrintzis, 'The use of Kirchhoff's method in computational aeroacoustics', in R.R. Mankbadi *et al.* (eds.), *Computational Aero- and Hydroacoustics*, vol. FED-147, ASME, 1993, pp. 53–61.
7. A.S. Lyrintzis and R.R. Mankbadi, 'Prediction of the far-field noise using Kirchhoff's formulation', *AIAA J.*, **34**, 413–416 (1996).
8. J.C. Hardin, 'Recent insights into computational aeroacoustics', in R.R. Mankbadi *et al.* (eds.), *Computational Aero- and Hydroacoustics*, vol. FED-147, ASME, 1993, p. 1.
9. K. Viswanathan and L.N. Sankar, 'Numerical simulation of airfoil noise', in A.S. Lyrintzis *et al.* (eds.), *Computational Aeroacoustics*, vol. FED-219, ASME, 1995, pp. 65–70.
10. G.S. Djambazov, C.-H. Lai and K.A. Pericleous, 'Development of a domain decomposition method for computational aeroacoustics', *DD9 Proceedings*, Wiley, New York, 1997.
11. G.S. Djambazov, C.-H. Lai and K.A. Pericleous, 'Domain decomposition methods for some aerodynamic noise problems', *3rd AIAA/CEAS Aeroacoustics Conference, No. 97-1608*, 1997, pp. 191–198.
12. G.S. Djambazov, C.-H. Lai and K.A. Pericleous, 'Efficient computation of aerodynamic noise', *Contemporary Mathematics*, vol. 218, American Mathematical Society, 1998, pp. 506–512.
13. *PHOENICS*, CHAM Ltd., Wimbledon, UK.
14. N. Croft, K. Pericleous and M. Cross, 'PHYSICA: A multiphysics environment for complex flow processes' in C. Taylor *et al.* (eds.), *Numerical Methods in Laminar and Turbulent Flow '95*, vol. 9, part 2, Pineridge Press, UK, 1995, p. 1269.
15. G.S. Djambazov, C.-H. Lai and K.A. Pericleous, 'Testing a linear propagation module on some acoustic scattering problems', in: C.K.W. Tam and J.C. Hardin (eds.), *Second Computational Aeroacoustics Workshop on Benchmark Problems, No. 3352*, Conference Publications, NASA, 1997, pp. 221–229.
16. A.T. Degani and G.C. Fox, 'Parallel multigrid computation of the unsteady incompressible Navier–Stokes equations', *J. Comput. Phys.*, **128**, 223–236 (1996).
17. K.A. Kurbatskii, 'Analytical solutions of the category 1, benchmark problems 1 and 2', in C.K.W. Tam and J.C. Hardin (eds.), *Second Computational Aeroacoustics Workshop on Benchmark Problems, No. 3352*, Conference Publications, NASA, 1997, pp. 9–14.